

Chapter 13

Depth Profiling and Internal Structure Determination of Low Dimensional Materials Using X-ray Photoelectron Spectroscopy

Sumanta Mukherjee, Pralay K. Santra and D.D. Sarma

Abstract Properties of any heterostructured material depend critically on the specific composition profile of the constituent elements in the sample. X-ray photoelectron spectroscopy (XPS) is particularly well suited to probe elemental composition of any system. Tunable photon energies, available from any synchrotron centre, allow one to map out the compositional variation through a sample in a manner that can be termed non-invasive and non-destructive depth profiling. In addition, XPS is also able to provide depth resolved electronic structure information by directly mapping out occupied states at and near the Fermi energy. Recent developments at various synchrotron centers, providing access up to very high energy (~ 10 keV) photons with a good resolution and flux, have made it possible to estimate such compositional and electronic structure depth profiles with a greater accuracy for a wider range of materials. In this book chapter, we describe in detail the use of X-ray photoelectron spectroscopy in a selection of heterostructures, in order to illustrate the power of this technique.

S. Mukherjee · P.K. Santra · D.D. Sarma (✉)
Solid State and Structural Chemistry Unit, Indian Institute of Science,
Bengaluru 560012, India
e-mail: sarma@sscu.iisc.ernet.in

P.K. Santra
Department of Chemical Engineering, Stanford University, Stanford, USA

D.D. Sarma
Department of Physics and Astronomy, Uppsala University, Box 534,
Uppsala 751 21, Sweden

13.1 Introduction

Tailoring functionalities by constraining dimensionalities of materials, typically down to the range of a few nanometers, has become a well-developed field over the last few decades [1–3]. Major technological advancement in diverse fields such as electronics, robotics, alternative energy sources, catalysis, sensor technology, aeronautics, medical diagnostics and therapeutics are dependent on the ability to control material synthesis at such extremely small sizes. Since most material properties are highly size-sensitive at such small length scales [3–6], there has been an enormous effort to design and optimize synthesis for a precise control of the size [4, 7, 8] and shape [9–13] of various materials. Apart from the control of size and shapes, a large variety of heterostructured nanoparticles [14–24] with diverse internal structures (or composition profiles) has also been produced to meet specific requirements for a range of applications. A few examples are coating of silica on certain functional nanomaterial to make them water soluble [25], a requisite for medical usage or a coating of high bandgap semiconductor nanomaterial on a low band gap nanomaterial to obtain better photophysical properties [19, 26]. Core/shell [5, 14–18, 27–29], homogeneous and heterogeneous alloy [19, 30–32], core/shell/shell [20, 21, 33, 34], and coupled dots [22, 23] are some more examples of diversity of internal structures in such heterostructured systems, which are becoming increasingly popular to improve their specific properties. It is easy to anticipate that enhanced desirable properties achieved via the synthesis of different heterostructures mentioned above must be controlled by the variation of different constituent elements across the heterostructure. For example, properties of a simple core-shell material with a sharp boundary between the core and shell materials are expected to be different from a core-shell material having alloying/mixing across the core/shell interface. Many a times, the structure of a synthesized nanomaterial is implicitly assumed to be the one targeted by the specific synthesis strategy, with evidences being drawn from a variety of indirect techniques, *e.g.* by monitoring the changes in position of the photoluminescence (PL) peak in case of a core-shell nanoparticle system [18]. It has been illustrated [19, 20] in recent times that, such assumptions are not always valid. On the other hand slight changes in the composition profile across the interface of the synthesized nanomaterial were shown to markedly alter certain properties *e.g.* PL properties and PL intermittency [19, 35–39]. Therefore, it becomes necessary to have a detailed knowledge of the internal structure of such materials [19, 35–37] in order to, not only understand the origin of extraordinary properties of such nanomaterials with a possibility of complex internal structures, but also to tailor synthesis for improved targeted properties based on rational approaches arising from that understanding.

As in the case of nanomaterials discussed above, internal structure in terms of composition profile of different constituents is also important in various two-dimensional (2D) multilayered thin film heterojunctions, specifically, where interface characteristics are important in controlling specific properties. Probably the most remarkable example of such heterostructures are 2D thin films semiconductor

heterostructures forming diodes and transistors, which are integral parts of all electronic devices. Other examples include tunneling magneto-resistance (TMR) based modern day magnetic devices, where interface play an important role controlling the coherency of tunneling current in such systems [40–44]. Among various 2D thin film electronic devices, one of the most exciting and emerging research fields is the heterostructure of various oxide materials, where a rich variety of unexpected phenomena has been observed in recent times [45–48]. One such example is the interface between two insulating nonmagnetic oxides, namely LaAlO_3 and SrTiO_3 , which shows properties ranging from high mobility metals to superconductivity and magnetism [45, 48–50] depending on the specific synthesis conditions. This underlines once again the need to understand the interfaces of heterostructures in depth and greater details.

In this book chapter, we discuss an unconventional way of determining the composition profiles in complex heterogeneous low dimensional materials (nanoparticles, thin films) using variable kinetic energy X-ray photoelectron spectroscopy (XPS), which has become an important technique with recent improvement in various synchrotron centers providing high and widely tunable photon energies with high fluxes and resolutions [51–61]. This chapter is divided in three main sections: (a) basic principle and common use of XPS in studying different nanoparticle and thin film systems; (b) principle of variable energy XPS to determine the internal composition profile of complex nanostructures with a few examples and understanding different optoelectronic properties from the derived internal structure; and (c) usefulness of recently developed hard X-ray photoelectron spectroscopy (HAXPES) [51–61] in determining the internal interface structure of nanoparticles and thin film heterostructures. Finally, we end this book chapter with a conclusion and future outlook section.

13.2 X-ray Photoelectron Spectroscopy and Early Applications in Studying Nanoparticles

X-ray photoelectron spectroscopy (XPS), a highly surface sensitive technique, is an established tool to determine the electronic structure of various materials. Since the method of photoelectron spectroscopy is directly related to the electronic energy states of a material, it can give many useful information like charge, valence state, band structures etc. besides identifying the elemental composition in the sample volume that it probes. The basic principle of XPS is related to the photoelectric effect [62]. In this technique, monochromatic photons of known energy are irradiated on the sample, leading to absorption of the photon by a bound electron and causing its emission; this process of ejecting *photoelectrons* happens for all electronic energy levels of all elements present in the material with different probabilities, characterized by the corresponding photoemission cross-sections, provided the photon energy is larger than the binding energy of that level including the work

function of the material. Let us assume that on absorbing a photon with sufficient energy, $h\nu$, an electron from one of the occupied energy levels, with a binding energy of BE , is ejected from the system with a kinetic energy of KE . The kinetic energy of the ejected photoelectron, is related to its BE as shown in (13.1)

$$KE = h\nu - (BE + \phi) \quad (13.1)$$

where ϕ is the work function of the spectrometer. Therefore, by measuring the KE of the photoelectron, the BE of the electron prior to the photoionization process can be determined. The BE of a photoelectron emitted from a specific electronic energy level of an element in a sample depends on the chemical state of the element in the given material. Even small changes in the chemical environment can influence the BE and such changes in the BE of an electronic level arising from the change in the chemical environment around the specific element is known as chemical shift [63, 64], which is often characteristic of the valence state or effective charge state of the element in the given material within a related family of compounds. This particular way of using chemical shifts to determine chemical states of different elements in matters has been so extensively used that the technique is often termed separately as ‘electron spectroscopy for chemical analysis’ (or popularly known as ESCA) [63, 64]. Sokolowski et al. have discussed the development of ESCA in Chap. 2 of this book in details.

With a decrease in the size of any material, the surface-to-bulk ratio increases, enhancing contributions from the surface to every property compared to its bulk contribution. Thus, a detailed knowledge of surface properties becomes essential to understand such low dimensional systems. Being one of the most surface sensitive techniques, XPS has become a very useful tool to characterize electronic structures of materials of lower dimensionalities. It has been applied very frequently to qualitatively ascertain the formation [15, 65–67] and the quality of the synthesized nanoparticles as well as to understand their surface characteristics and compositions [67–76]. A few illustrative examples of the use of XPS in nanoparticle systems are discussed below.

In one of the earliest investigations on the effect of a decreasing size on the metallicity of Pd and Ag nanoclusters, Vijayakrishnan et al. used XPS to show that decreasing sizes lead to an opening of band gap at the Fermi level below a critical size of the nanoclusters, evidencing a characteristics of metal-insulator transitions in such systems [77]. In another XPS study [71] of PbI_2 nanoparticles, a huge excess of I 3d signal was observed compared to Pb 4f, which suggests that iodide ions plays an important role in stabilizing the PbI_2 nanocrystallites in different solvents. Roy et al. used XPS in conjunction with step-wise argon-ion etching of the surface of a luminescent porous silicon sample to probe the composition in the surface and sub-surface region [70]. However, it is to be noted that this approach can only provide qualitative and often relative information and is not reliable to quantify the results with a great accuracy due to the preferential etching of certain elements compared to others. Jasieniak et al. have used different techniques to synthesize either Cd or Se rich CdSe nanoparticles and the formation of such nanoparticles

were confirmed from the core level photoelectron spectra of Cd 3d or S 2p [72], which shows additional features related to the presence of excess Cd or Se at the surface of such nanocrystal systems. In a similar study on Cd rich CdSe nanoparticles [76], XPS was used to extract the composition of the surface with excess Cd, which was shown to be crucial to optimize the PL efficiency of those nanoparticle systems. XPS has also been used to understand the surface passivation of nanoparticles by various organic ligands, often used for better stability and good size distribution of nanoparticles. XPS studies of trioctylphosphine oxide (TOPO) passivated CdSe nanoparticles of different sizes revealed evidence for the surface binding of TOPO only to the surface Cd, leaving the surface Se intact; this was further supported by the observation of preferential oxidation of Se [73]. XPS chemical shift has often been used to characterize attachment between two different kinds of nanoparticle systems for example Au with TiO₂ or MoO₃ with TiO₂ [78, 79], such complex systems being specifically required for applications in catalysis or in photovoltaic solar cells. In one of the earliest use of synchrotron radiation to carry out variable energy XPS of semiconductor nanocrystals, Kulkarni et al. showed the presence of different S species on CdS nanoparticles stabilized with thioglycerol as the passivating agent [74, 75]. In the same way, many qualitative information like formation, surface chemistry, elemental composition, and interfacial carrier dynamics under photo irradiation have also been obtained from various heterostructured nanoparticles systems using XPS.

13.3 Description of the Internal Structure Using XPS

In general, XPS studies including few examples mentioned above, did not involve any *quantitative* determination of the internal structure, say of a nanoparticle. Common characterization techniques, like transmission electron microscopy (TEM) [28], X-ray diffraction (XRD), photoluminescence emission spectroscopy, Raman spectroscopy [36, 80, 81] etc. have been used to probe the internal structure, but these provide only qualitative information about the internal structure. More advanced techniques such as scanning transmission electron microscopy (STEM) coupled with either energy dispersive X-ray spectroscopy (EDX) or electron energy loss spectroscopy (EELS) can provide more quantitative information on the compositional variation across interfaces in some specific cases [82]. In certain 2D thin film heterostructures, high angle annular dark field (HAADF) imaging in TEM can also provide information on the elemental distribution [49]. In the following sections, we shall describe a nontraditional use of XPS to *quantitatively* determine the internal structure of a variety of heterostructures.

While different nondestructive and quantitative methods [83–92] of determining internal structures of a number of systems have been developed using XPS over the last few decades, we shall discuss in greater details one such method [88] that is versatile, having been applied to a wide variety of systems, discussing more briefly the other methods wherever relevant.

The quantitative determination of the internal structure of a heterostructure relies on the intensity [88, 93–97] of the photoemission signal arising from different energy levels of all elements present in the sample. In XPS, the photoemission signal intensity depends on various parameters as discussed in the following. In order to be detected as a photoemission signal, the photoelectron must travel from the atomic site of photoabsorption to the analyzer without suffering any inelastic process according to the energy conservation indicated by (13.1). During this travel through the material, the photoelectron has a finite probability to interact with the sample, for example, with other electrons present. These collisions can be elastic, thus retaining the same KE of the photoelectron and thereby contributing to the photoelectron spectra. Alternately, these can also be inelastic, which causes a decrease in the photoelectron KE ; such electrons are lost from the main photoelectron spectra being detected as the background [98, 99] of the photoemission signal. These processes are schematically shown in Fig. 13.1a. The probability of the inelastic scattering, can be defined in terms of the average distance, λ , between two inelastic collisions for the same photoelectron, thus defining a mean free path of the photoelectron. The probability of a photoelectron coming out from the sample without any inelastic scattering follows an exponential dependence on the depth at which the original photoabsorption process takes place, and with that the differential photoemission signal intensity, $dI_{z'}$, originating from a volume of ' dv ' at a depth z' from the surface can be expressed as [88, 93–96]

$$dI_{z'} = I_0 \exp\left(\frac{-l}{\lambda}\right) dv = I_0 \exp\left(\frac{-z'}{\lambda \cos \alpha}\right) dv \quad (13.2)$$

where, ' l ' is the path length of the photoelectron to travel to the surface of the material from the originating point in the direction of the electron analyzer and α is

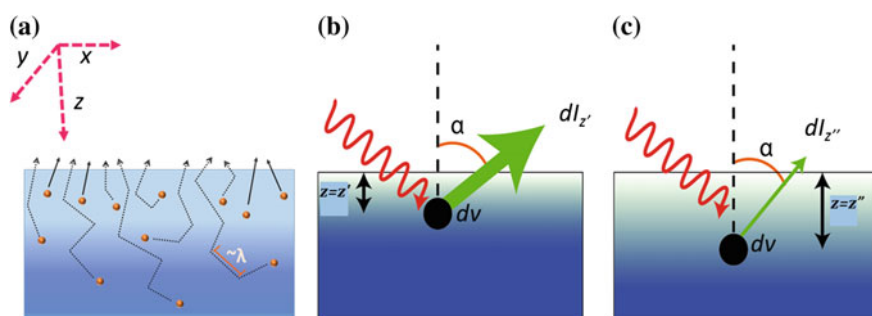


Fig. 13.1 **a** Schematic illustration showing the increasing probability of collision of photoelectrons with increasing depth of their generation, thereby, decreasing their escaping probability exponentially. The average length scale, λ , represents the mean free path of the photoelectrons. **b** and **c** Photoelectrons generated from a volume element ' dv ' present at different depth, z' and z'' , from the surface of the material show different intensities in the photoemission signal, with the intensity dropping off exponentially with z . Adapted from [88]

the angle between the electron detection and surface normal; I_0 is the proportionality constant dependent on various factors, such as the photon flux (P), transmission function of the spectrometer, and the photoemission cross-section (σ) or the photoionization probability for the atomic level in question (Fig. 13.1b). It is clear from the above equation that the differential contribution dI to the total intensity I of a particular electronic energy level (core level) decreases exponentially with an increase in z , and consequently, $\sim 95\%$ of the total photoemission signal comes from the surface region of 3λ thickness if the angle of detection (α) is considered to be zero. The remaining 5% originates from the region deeper into the sample. While this immediately explains the surface sensitive nature of the XPS technique (λ being in the range of few nm), it is interesting to note here that increasing the angle of detection with respect to the surface normal makes it even more surface sensitive, since the photoelectron then needs to escape more tangential to the surface, therefore, requiring a longer path length (l) within the material for the same depth z' as shown in Fig. 13.1b. For example, for $\alpha = 45^\circ$, a 3λ thick surface region contributes as much as 98.5% of the total signal. It is also clear from (13.2) that the surface vs bulk sensitivity of this technique can also be controlled by systematically changing the mean free path λ of the photoelectron, as can indeed be done by changing the photon energy, $h\nu$; we shall discuss this aspect in the next section of this chapter. The total intensity, I , of the photoelectron signal of a particular core level at a given photon energy, $h\nu$, including all parameters can be obtained by integrating (13.2) over the entire volume and expressing I_0 in terms of its component parameters, as given below

$$I(h\nu) \propto K \cdot P(h\nu) \cdot T(KE)\sigma(h\nu) \int_v N(x, y, z) \exp\left(\frac{-z}{\lambda(KE) \cos \alpha}\right) dx dy dz \quad (13.3)$$

where the prefactor K takes care of the geometry of the measurements (such as the angular acceptance of the analyzer), P is the flux of the incident photon beam and T is the transmission function of the analyzer. The parameters K , P and T are characteristics of the instrument and measurement conditions, the sample specific information is coded in the parameter $N(x, y, z)$, the number density of the specific element distributed in the sample, in addition to the parameter $\sigma(h\nu)$, representing the $h\nu$ -dependent photoionization cross-section of the specific core level of the element in question. It is obvious that the distribution, $N(x, y, z)$, of all elements define the internal structure of any given sample. Therefore, the problem of determining the internal structure reduces to extracting $N(x, y, z)$ from the photoemission signal. Since photoemission signals are sensitive to the chemical state of the element probed, variable energy XPS not only can provide the internal structure in terms of mapping the elemental distribution, it can also provide information on the chemical state of the element with spatial resolution, as will be discussed in the following sections.

13.4 Inelastic Mean Free Path, λ , of Photoelectrons

As mentioned earlier, the mean free path, λ , of the photoelectron is the average distance between two inelastic collisions and it depends on the KE of the photoelectron. The dependency of λ with KE can be given approximately by Wagner, Davis and Riggs equation [100] as

$$\lambda \approx m (KE)^n \quad (13.4)$$

when KE is expressed in electronvolt (eV) and λ in angstroms (\AA). This purely empirical equation with ($m = 0.5$ and $n = 0.5$) is found to be reasonably valid for a wide range of KE above ~ 150 eV in the soft X-ray region (<1000 eV). While for very high KE regions (>2000 eV) the values for m and n are found to be ~ 0.11 and ~ 0.75 [100–102]. There are several other ways to calculate the mean free path of the photoelectron, for example using TPP and TPP-2 formula [100, 103, 104]; these have been discussed in Chap. 5 by Powell and Tanuma. For a specific core level of an element in a given sample, it is easy to change the KE of the photoelectron by changing the incident $h\nu$ according to (13.1); this implies that $\lambda(h\nu)$ varies approximately as $(h\nu - BE)^n$ and therefore, can be tuned by suitable choice of $h\nu$. With recent advancement on the synchrotron sources, it is possible to tune the photon energy almost continuously over a wide range, thereby achieving a continuous tuning of the KE and λ of any photoelectron originating from any specific core level. In the early days of photoelectron spectroscopy, λ values typically ranged from 0.5 to 2 nm ($3\lambda_{max} \sim 6$ nm) depending on the BE of the core level with the use of laboratory sources like Al $K\alpha$ (1486.6 eV) and Mg $K\alpha$ (1253.4 eV); presently, with the advent of sophisticated synchrotron facilities, the possibility of continuously varying λ using such variable photon energy source forms the main basis of mapping out the chemical compositions, defined by $N(x, y, z)$ of all the elements, at various depths within the sample, thereby enabling characterization of the internal structure of a large number of systems. We have pointed out earlier that it is possible to change the *effective* mean free path ($\lambda \cdot \cos\alpha$) by varying the detection angle, α , keeping $h\nu$ (and consequently, λ) at a fixed value. This method of internal elemental composition mapping by varying the detection angle has often been used for internal structure determination of thin films [90, 91, 105]. While such method has inherent limitations [91, 102] and suitable only when the 2D film thickness to be estimated is considerably smaller than the λ of the photoelectrons [90, 102], the alternate method [88, 102] of using variable $h\nu$ is robust and applicable to a wide variety of geometry, for example for spherically shaped nanoparticle systems where the method based on variation of detection angle, α would be ineffective.

13.5 Intensity Variation of Different Core Levels/Elements with photon energy, $h\nu$, in Heterostructures

The idea to probe a sample at different depths using variable energy XPS has been explained [88] in this section with the help of schematic Fig. 13.1. Let us consider the absorption of a photon with sufficient energy of $h\nu$ at a depth of z' from the sample surface, thereby causing emission of a photoelectron that is detected with an intensity of $dI_{z'}$ at an angle of α from the surface normal, as shown in Fig. 13.1b. With no loss in generality, let us consider that another photon with same energy $h\nu$, causes a photoelectron from another atom of the same element and core level to originate at a depth of z'' and detected with an intensity of $dI_{z''}$ at the same angle of α from the surface normal as shown in Fig. 13.1c. From (13.2), the intensity ratio of the two photoelectrons originating at two different depths can be expressed as

$$\frac{dI_{z'}}{dI_{z''}}(h\nu) = \exp\left(\frac{z'' - z'}{\lambda(h\nu) \cos \alpha}\right) \quad (13.5)$$

As $z'' > z'$, the intensity contribution from the deeper volume element at z'' , will be lower compared to that from z' ($dI_{z''} < dI_{z'}$). The above equation also shows that an increase in λ by increasing $h\nu$ will lead to a systematic decrease in the intensity ratio $\frac{dI_{z'}}{dI_{z''}}(h\nu)$, due to an increase in the relative contribution from the deeper region of the sample compared to regions that are closer to the surface. Now, instead of one element if the sample is made of two different elements **A** and **B** and the two volume elements at two different depths, z' and z'' contains the elements **A** and **B**, respectively, then in terms of total intensity contribution to the photoemission signals from some core levels (13.3) of the two elements, the intensity ratio can be written as

$$\frac{I_A}{I_B}(h\nu) = \frac{T_A}{T_B}(KE) \frac{\sigma_A}{\sigma_B}(h\nu) \frac{\int_V N_A(x, y, z) \exp\left(\frac{-z}{\lambda_A(KE) \cos \alpha}\right) dx dy dz}{\int_V N_B(x, y, z) \exp\left(\frac{-z}{\lambda_B(KE) \cos \alpha}\right) dx dy dz} \quad (13.6)$$

The immediate benefit of taking intensity ratio is that the contributions of uncertain instrumental factors, (e.g. K , P), mentioned earlier in (13.3), are not required to be considered any more, the expression for the intensity ratio being independent of those factors. The remaining parameters, namely the transmission functions T 's and cross-sections, σ 's in (13.6) can be estimated as a function of $h\nu$ [106–108], leaving only the number densities $N_A(x, y, z)$ and $N_B(x, y, z)$ as the unknown variables. It is clear from (13.6) that, for different heterostructures, characterized by different number density profile of the constituent elements, the variation of intensity ratio I_A/I_B as a function of $h\nu$ will be different, and by measuring I_A/I_B at many different $h\nu$, it is possible to determine the number densities, defining the internal structure of a given heterostructure. This is further illustrated in

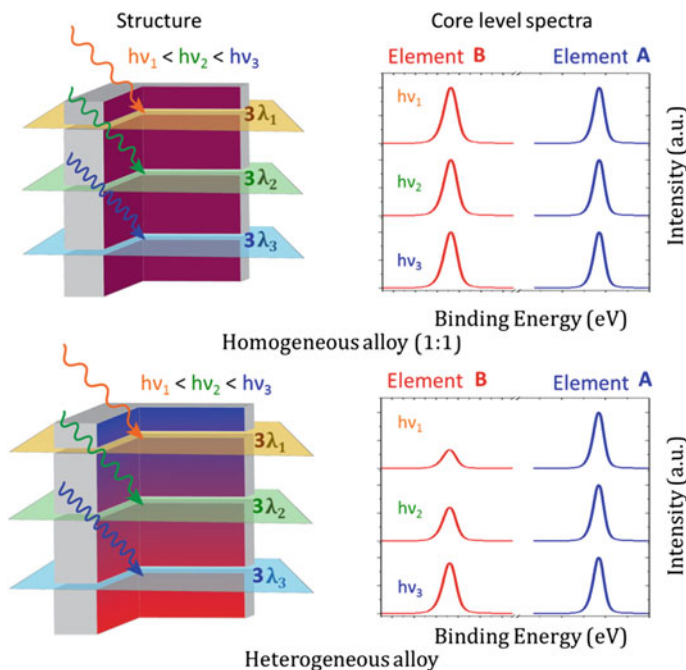


Fig. 13.2 Schematic illustration of spectral dependence on photon energy for two systems having different internal structures. One system is chosen to represent a homogeneous alloy of two elements (say **A**, indicated in *blue color* and **B**, indicated in *red color*), while the other one has a graded alloy structure with the core rich in **B** and the surface in **A**. The graphs on the *right side* show schematically changes in the relative intensities with increasing photon energy. Horizontal slices from the *top* represents changing mean escape depth, λ , with a changing photon energy where $hv_1 < hv_2 < hv_3$, giving rise to $\lambda_1 < \lambda_2 < \lambda_3$. Adapted from [88]

the Fig. 13.2, where we have considered two hypothetical materials with flat surfaces consisting of two elements **A** (indicated by blue) and **B** (indicated by red). For the sake of simplicity, let us consider that the photoemission cross-sections of the specific core levels of these two elements σ_A and σ_B are equal and also the *KE* of the emitted photoelectrons have similar values and, therefore, $T_A = T_B$ and $\lambda_A = \lambda_B = \lambda$ in (13.6). In the first scenario, we consider our hypothetical material to be a homogenous alloy of elements **A** and **B**, implying that these elements are distributed uniformly within the material, as shown in the upper left schematics. The other hypothetical material also consists of elements **A** and **B**, but they form a gradient alloy structure with only element **A** on the surface and only element **B** at a certain depth with the composition changing uniformly in-between. With a low photon energy of hv_1 , the primary contribution to the photoemission signal will come from a thin slice of the sample, as shown in the Fig. 13.2, with the slice thickness governed by the mean free path, λ_1 , of the photoelectron with the photon energy of hv_1 . In case of the homogenous alloy, the intensity ratio of core levels of **A** and **B**, I_A/I_B will be independent of hv , as can be seen from (13.6) with

$N_A(x, y, z)/N_B(x, y, z)$ being a constant dependent only on the composition of the homogeneous alloy, but independent of x , y , and z over the entire volume of the sample.

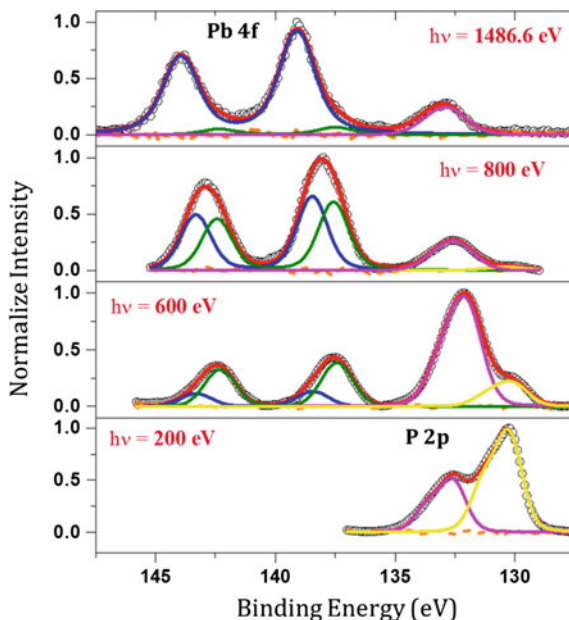
However, the same intensity ratio will be critically dependent on $h\nu$ in case of the graded alloy sample with $N_A(x, y, z)/N_B(x, y, z)$ being dependent on z ; clearly for a small λ_1 , the thin slice probed in the experiment contains a dominant contribution of **A** as illustrated in Fig. 13.2 for the graded alloy structure with the blue color representing the element **A**. Thus, the photoemission signal will be largely dominated by the contribution of **A** with a smaller contribution from **B** with the lowest photon energy of $h\nu_1$. With a progressive increase in the photon energy ($h\nu_3 > h\nu_2 > h\nu_1$), the mean free path of the photoelectrons will also increase ($\lambda_3 > \lambda_2 > \lambda_1$). The intensity ratio I_A/I_B will not change with photon energy for the homogeneous alloy, as shown in upper right schematic spectral distribution. However, the relative intensity ratio I_A/I_B will increase with increasing photon energy for the gradient alloy (lower right schematic graph). From this illustrative example, it is clear that the variation in signal intensity ratio of different elements obtained at different $h\nu$ will provide information of the internal structure of the materials with dimensions comparable to the mean free path (λ) of the photoelectrons. It is important to note here that a heterostructure does not necessarily need two different elements, it can be made of different spatial distribution of two different chemical states (**A** and **A'**) (for example different valence states), characterized by a slightly different BE (chemical shift) of the same core level spectra, of one element (**A**). In such situations (13.6) will have the following form

$$\frac{I_A}{I_{A'}}(h\nu) = \frac{\int_V N_A(x, y, z) \exp\left(\frac{-z}{\lambda(KE)\cos\alpha}\right) dx dy dz}{\int_V N_{A'}(x, y, z) \exp\left(\frac{-z}{\lambda(KE)\cos\alpha}\right) dx dy dz} \quad (13.7)$$

and can be used the same way for internal structure determination. We shall provide examples of each of the situations described above in the following sections.

At this stage we provide a real illustrative example, to show the sensitivity of this approach in delineating complex nanostructures with additional information coming from the phenomenon of chemical shift that was alluded to earlier in this chapter. We adopt results from [109] and a sequence of photoemission signals from PbSe nanocrystals passivated with TOPO in Fig. 13.3 for a series of photon energy. The two peaks apparently at 130 and 132.8 eV binding energies are both associated with P 2p core level from TOPO. It is clear from the spectra, the P related intensities are dominant in the extremely surface sensitive limit of low photon energies, establishing P to be present predominantly at the surface of the sample. This is consistent with TOPO being a superficial capping agent for these nanocrystals. Interestingly, the chemically shifted two P 2p core level signals appearing at 130 and 132.8 eV show different dependencies on the photon energy; specifically, the peak with the lower BE of 130 eV clearly corresponds to a more surface species compared to the features at the higher BE of 132.8 eV. This fact, together with the observed

Fig. 13.3 High-resolution photoemission spectra of the Pb 4f and P 2p core levels collected at various photon energies from PbSe nanoparticles. Contributions to Pb 4f spectra arising from distinct Pb species are shown in *blue* and *green* lines along and those for P 2p are shown in *yellow* and *magenta* lines. Adapted from [109]



chemical shift, allows to assign the low *BE* feature to a physisorbed TOPO layer on top of the chemically bounded TOPO layer on the PbSe nanocrystal acting as the passivating agent. A careful analysis revealed [109] that the Pb 4f is also composed of two species of Pb with the one at lower *BE* being associate with the Pb near the nanocrystal surface and the other being located deeper into the volume of the nanocrystal. While this example makes clear the strength of this technique based on photoemission experiments with a variable energy source in providing unique insights in the internal structures of nanomaterials at a qualitative level, detailed examples are provided in the following section to illustrate how one may also extract quantitative information providing an accurate and detailed description of complex structures from such experiments.

13.6 Quantitative Determination of the Internal Structure

In the early days, XPS intensity ratios were extensively used to characterize as well as to estimate the thickness of various oxides formed on top of metallic samples [93, 94, 97, 110–113]. It was shown in [93] that with an increasing thickness of WO_3 layer deposited on top of metallic W the relative contribution to the W 4f XPS signal from the metallic W layer decreases with respect to WO_3 signal. While it was already suggested at that time that this relative change in the intensity ratio can be used to estimate the thickness of the top WO_3 layer; similar ideas were proposed

and pursued [110, 112, 113] to monitor quantitatively the progression of the oxidation process of various metals on increasing exposure to oxygen. Combining the concept of chemical shift, it was even possible to identify various species of oxides of Zr and follow their quantitative growth as a function of oxygen exposure in studies of oxidation of Zr and its alloys [94, 97]. Later this method of thickness estimation from the relative intensity ratios of photoemission signals was effectively implemented to determine the internal structure of various nanoparticles.

Nanda et al. [95] applied this method for a quantitative determination of the composition and the internal structure of different sized spherical CdS nanoparticles [95] capped with 1-thioglycerol. They investigated the internal structure using two different photon energy sources, namely, Al K α (1486.6 eV) and Mg K α (1253.4 eV). Both S 2s and 2p spectral features were found to be complex and could not be attributed to a single S species. Careful spectral decompositions of both S 2p and S 2s spectra showed evidence for three distinctive features suggesting three different S species present in the CdS nanoparticles. For example, three different S 2p_{3/2} peaks were found to be at about 161.8, 162.9 and 163.9 eV binding energies, representing three chemically shifted signals. These three S components were attributed to S in the bulk of the CdS nanoparticle, S at the surface layer of CdS and the S present in the thiol group of the capping agent, 1-thioglycerol, respectively. While the S species in the thiol group with a very different chemical environment is indeed expected to give rise to a strong chemical shift compared to S species in the nanoparticle as observed, the shift in the S 2p core levels from the S atoms at the surface of the nanoparticle compared to those in the bulk is known as the surface chemical shift. The surface nature of that specific S component was further confirmed by studying two different sizes of CdS nanoparticles synthesized in the same way. It was found that the second component of S species attributed to the surface layer had a higher contribution relative to the first component assigned to the bulk for the smaller nanoparticle, as should indeed be expected on the basis of an increasing surface to bulk ratio with a decrease in the size. Yet another validation of this interpretation was provided by the use of Mg K α (1253.4 eV) as the photon source to carry out XPS with a slightly smaller photon energy on the same nanoparticles. The results with Mg K α (1253.4 eV) again exhibited the same three components of S species, however, with an increased contribution of both second (surface) and third (thiol) components, relative to the first one. This is a consequence of the lower photon energy of Mg K α (1253.4 eV) source compared to Al K α (1484.6 eV) one, leading to a lower λ and consequently a higher surface sensitivity with Mg K α (1253.4 eV) radiation. The internal structure of the CdS nanoparticles was modeled as a core/shell/shell structure with a CdS core, a surface CdS layer and finally, the capping layer of 1 thioglycerol as shown schematically in Fig. 13.4 with radii of r_0 , r_1 and r_2 , respectively, yielding the detailed structure of these nanoparticles. They modify and express (13.7) in a spherical polar coordinate to estimate the intensity ratios between different S components mentioned above. The exact values of the radii were calculated by varying these radii parametrically to simulate the experimentally obtained signal intensity ratio of three different components S 2p at different photon energies. In a different study [96] to determine

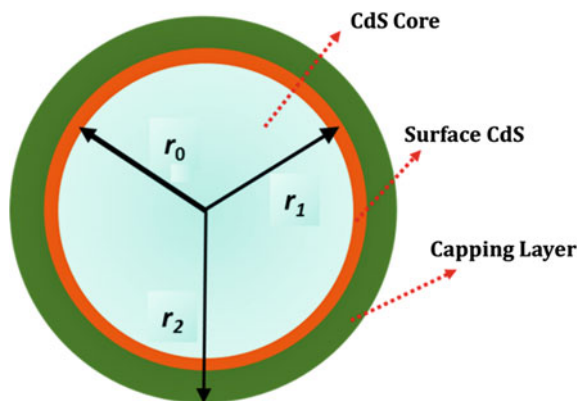


Fig. 13.4 Schematic model of CdS nanoparticles as derived from XPS analysis showing a CdS core region till r_0 , followed by a thin shell of surface CdS layer of thickness $(r_1 - r_0)$. Surface S atoms exhibit a different core level binding energy due to what is known as surface core level shift. Finally, there is a protective layer of capping agent (thiol) of thickness $(r_2 - r_1)$ on the top. Adapted from [95]

the internal structure of ZnS nanoparticles passivated with 1-thioglycerol, XPS at various photon energies suggested the internal structure of these ZnS nanoparticles being similar to the internal structure of the above-mentioned CdS nanoparticles. The generality of this approach was demonstrated by Sapra et al. [109] who used variable energy XPS to determine the internal structure of luminescent PbSe nanoparticles as well as of nanorods by modifying (13.7) and expressing it in cylindrical polar coordinates. The variable energy XPS study [109] on different sized PbSe nanoparticles (Fig. 13.3) have suggested formation of Pb deficient Pb_{1-x}Se layer on the surface of these nanoparticles. The thickness of this Pb deficient layer was found to be smaller for smaller sized nanoparticles. As the Pb deficient layer leads to the formation of trap states, which decreases the photoluminescence efficiency, they were able to explain the optoelectronic properties of the studied PbSe nanoparticles on the basis of internal structure and surface properties [109]. This later example illustrates the usefulness of the aforementioned variable energy XPS technique in correlating properties of lower dimensional materials with their internal structures.

Similar analyses can also be performed on nanoparticles with complex heterostructures with complicated variations in the composition. Unlike in the examples cited above, more complicated multicomponent structures require monitoring photoelectron signals of more than one element to accurately profile the composition through the nanoparticle, as has been discussed in previous sections. In recent times, there has been many reports [19, 20, 33, 114–116] using high quality and continuously tunable synchrotron photon sources on complex nanostructures. For example, Santra et al. [20] determined the internal structure of a targeted core/shell/shell ZnS/CdSe/ZnS quantum dot–quantum well (QDQW) structure. They analyzed the intensity ratio of S 2p and Se 3p core level spectra collected at

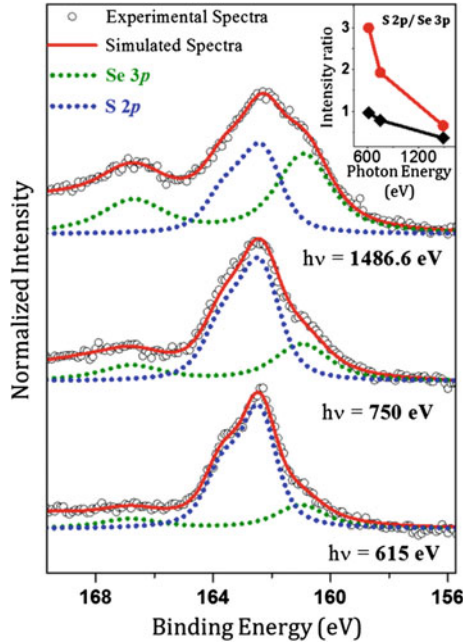


Fig. 13.5 High-resolution photoemission spectra of the S 2p and Se 3p core levels at various energies. At each energy, the experimental data are shown by the *black circles* and the total fit by the *red line*. The independent component functions, S 2p and Se 3p are shown as *blue* and *olive dotted lines*, respectively. The *inset* shows the S 2p/Se 3p intensity ratios obtained with (*red circles*) and without (*black square*) consideration of the photoemission cross-section (the lines are guides to the eye). Adapted from [20]

three different energies. These two core levels were specifically chosen in view of the fact that binding energies of S $2p_{1/2}$ and $2p_{3/2}$ are very close to those of Se $3p_{1/2}$ and $3p_{3/2}$, as shown in Fig. 13.5. Having the similar binding energies, the KE of the S 2p and Se 3p photoelectrons are also similar, which allows recording of both the S 2p and Se 3p core levels simultaneously at any given $h\nu$. In view of very similar KE for both peaks at a given $h\nu$, it is reasonable to assume that K , P and T , mentioned in (13.3), are same for both S 2p and Se 3p core level at a given $h\nu$, and are exactly cancelled in the intensity ratio between S 2p and Se 3p core level spectra. The inset to Fig. 13.5 shows the experimental intensity ratio obtained by the decomposition of the recorded spectra in terms of S 2p and Se 3p contributions, as shown in the main frame by dotted lines. Equation (13.8) can be derived from (13.6), in a spherical polar coordinate for the intensity ratio of S 2p and Se 3p as:

$$\frac{I_S}{I_{Se}} = \frac{\int_v dI_S}{\int_v dI_{Se}} = \frac{\sigma_S \int_0^R \int_0^\pi \int_0^{2\pi} N_S(r) \exp\left(-\frac{f(r,\theta)}{\lambda}\right) r^2 \sin(\theta) d\theta d\varphi dr}{\sigma_{Se} \int_0^R \int_0^\pi \int_0^{2\pi} N_{Se}(r) \exp\left(-\frac{f(r,\theta)}{\lambda}\right) r^2 \sin(\theta) d\theta d\varphi dr} \quad (13.8)$$

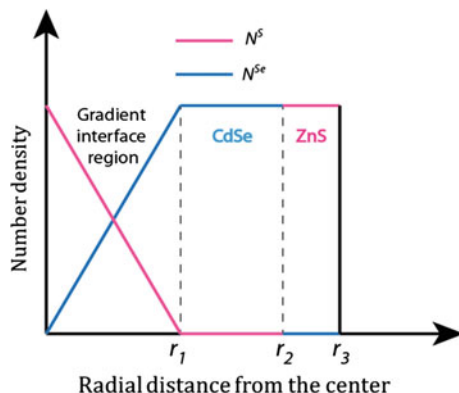


Fig. 13.6 Schematic representation of the variation of the chemical composition for the best fitted structure, which has three main layers: a gradient alloy in the core ($0 < r < r_1$) followed by a thick shell of CdSe ($r_1 < r < r_2$) and a thinner shell of ZnS ($r_2 < r < r_3$). Adapted from [20]

where, R is the total radius of the nanoparticle, mean free paths (λ_S and λ_{Se}) of S 2p and Se 3p photoelectrons with almost the same KE for any given $h\nu$ are essentially the same and therefore, has been replaced with λ ($= \lambda_S = \lambda_{Se}$) in (13.8). The quantity $f(r, \theta)$ is given by $f(r, \theta) = (R^2 - r^2 \sin^2 \theta)^{1/2} - r \cos \theta$. Equation (13.8), shows that the experimental intensity ratio obtained from the decomposition, after a suitable correction for the respective cross-sections, namely $(I_S/\sigma_S)/(I_{Se}/\sigma_{Se})$, is dependent on the elemental composition profile for S and Se, as expressed by $N_S(r)$ and $N_{Se}(r)$. Quantitative analyses of the photoemission data reveal that S and Se number densities for these QDQW nanoparticles varied as shown in Fig. 13.6, exhibiting the core region to be a graded alloy of ZnS and CdSe rather than pure ZnS as targeted. The solution based reaction to place a shell of CdSe on preformed ZnS nanocrystals is found to cause diffusion of Se ions towards the center of the nanoparticle, leading to the formation of such a gradient core. However, the outermost ZnS layer was found to form a sharp interface on top of the outer CdSe. The radius, r_3 , obtained from the analysis which corresponds to the total size of the nanoparticle was found to be in good agreement with results from TEM measurements. Also the chemical composition based on the model in Fig. 13.6 and extracted values of r_1, r_2 and r_3 , was found to be consistent with results from Inductively coupled plasma atomic emission spectroscopy (ICP-AES), thereby validating the photoemission analysis and estimates of r_1 and r_2 that would not be possible to obtain by any other technique.

In another interesting work to understand the extraordinarily high photoluminescence behavior of ternary CdSeS nanoparticles, the internal structure of these samples were determined [19] by analyzing the relative intensity variation of S 2p and Se 3p core levels at different photon energies in much the same way as in the previous example of QDQW. With additional information about the total size obtained from TEM and chemical composition from ICP-AES, internal structures

of such highly luminescent CdSeS nanoparticles were invariably found to consist of a gradient alloy structure of $\text{CdSe}_x\text{S}_{1-x}$ where x varies from 0 near the center of the nanoparticle to 1 near the surface of the nanoparticle. Depending upon the concentration ratio of S and Se used during the synthesis, the radius of the gradient core could be tuned to provide PL emission of different wavelengths spanning the visible spectrum. It was pointed out [19] that such a graded structure avoids any interface defect formation that tends to be present in systems with a sharp interface in core-shell structure due to the lattice mismatch. The absence of such interfacial defects in gradient structured CdSeS allows these nanoparticles to have a quantum yield as high as 80 %.

13.7 Hard X-ray Photoemission Spectroscopy (HAXPES)

While X-rays of very high energies, for example Cu $K\alpha$, have been used in photoemission experiments at very early days, the usage was limited due to the poor resolutions at that time [60]. The advancement in the third generation synchrotron radiation sources in recent times allows sufficiently high photon flux (P) with photon energies as high as 12 keV to carry out photoemission experiments with a good energy resolution. Therefore, it is now possible to tune the mean free path (λ) of the photoelectron up to ~ 10 nm. Such large mean free paths of the photoelectrons have opened up the possibility [51–61] of probing much greater depths and much larger nanocrystals that would have been otherwise impossible to probe with more conventional XPS.

Recently, Mukherjee et al. [117] employed such high energy XPS with $h\nu$ up to 4 keV in combination with surface sensitive lower energy XPS ($h\nu \geq 475$ eV) to elucidate the internal structure of inverted core-shell CdS-CdSe nanoparticles with an average diameter of 6 nm. Standard lab source (e.g. Al $K\alpha$ (1486.6 eV)) can generate photoelectrons with a mean free path of ~ 2 nm which is smaller than the size of these nanoparticles and therefore can give only restricted information. Instead, they [117] used a wide range of photon energies between 475 eV (thereby emphasizing the surface components) and 4000 eV (making the probe bulk sensitive) to study the core level intensity variation of overlapping S 2p and Se 3p spectra as shown in Fig. 13.7a. The benefit of using overlapping S 2p and Se 3p spectra has already been presented in the previous section of this book chapter. At lower photon energies, a distinct peak at 161.2 eV with a shoulder at 162.3 eV is dominant in the spectra. These binding energies correspond to $2p_{3/2}$ and $2p_{1/2}$ spin-orbit split 2p core levels of sulfur. There are also two low intensity peaks at 159.8 and 165.6 eV which correspond to Se $3p_{3/2}$ and Se $3p_{1/2}$ spectra with a spin orbit splitting of 5.8 eV. Interestingly, with an increase in $h\nu$, the Se 3p signal intensity increases significantly relative to the S 2p signal. This is most clearly evident when we follow the growth of the Se $3p_{1/2}$ spectral feature at 159.8 eV *BE* with changing $h\nu$; the corresponding enhancement of the Se $3p_{3/2}$ peak is less clear, as a worsening resolution with the increasing $h\nu$ makes it difficult to visually judge

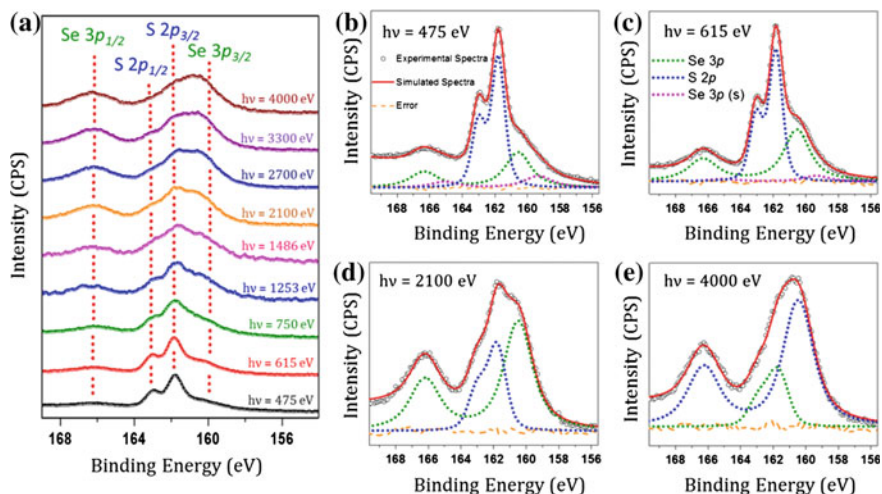


Fig. 13.7 **a** Photoelectron spectra of S 2p and Se 3p core levels collected at various photon energies from an inverted CdS/CdSe core-shell sample. **b–e** Decomposition of the experimental spectra (empty black circles) to different components, namely, the surface of Se 3p (olive), S 2p (blue), and Se 3p (s) (magenta). Red solid lines are the resulting fits, while the orange dashed lines are the residues. (Adapted from [117])

the contribution of Se 3p_{3/2} separate from those of S 2p_{3/2} and S 2p_{1/2} within the broadened main group around 160 eV BE (see Fig. 13.7a). However, it is easy to decompose each of the spectra in Fig. 13.7a in terms of contributions arising from S 2p_{3/2}, S 2p_{1/2}, Se 3p_{3/2} and Se 3p_{1/2} components as illustrated in Fig. 13.7b–e for a few selected photon energies [117]. Such spectral decompositions allow one to determine quantitatively the relative contributions of S and Se core levels in the overall spectra at different photon energies (Fig. 13.7a). Thus determined intensity ratio of the contributions from Se 3p and S 2p core level spectra is shown as a function of the photon energies in Fig. 13.8a by the solid blue squares, referred to the right axis, clearly showing the rapidly increasing Se 3p intensity relative to S 2p with an increasing $h\nu$. At this stage, it is important to note that the variation in the spectral intensities cannot be directly related to the variation in $N_S(r)$ and $N_{Se}(r)$ within the probing depth of the technique [see (13.8)], because the photoemission cross-section, σ , itself changes rapidly with $h\nu$ and its dependence on $h\nu$ is both element and core level specific. Therefore, we need to normalize the raw intensity ratio with the ratio of the photoemission cross-sections of Se 3p and S 2p levels for each of the photon energies [see (13.8)]. The corresponding cross-section corrected intensity ratios of Se 3p and S 2p are shown as a function of $h\nu$ in Fig. 13.8a with filled circles, referred to the left axis. Clearly, the corrections arising from the changing σ qualitatively alter the trend of the intensity ratio as a function of the $h\nu$ from an increasing to a decreasing function underlining the crucial importance of accounting for changes in $\sigma(h\nu)$ even for a qualitative understanding of chemical composition as a function of the probing depth in any given material.

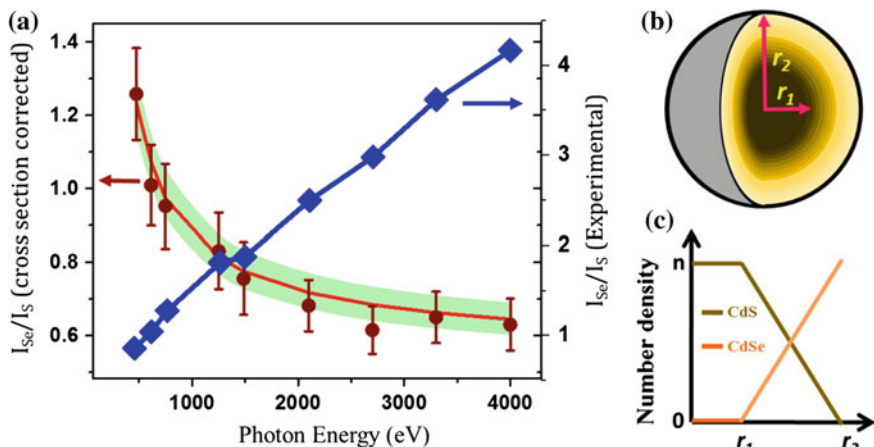


Fig. 13.8 **a** Variation of the experimental (blue squares joined by a blue line) and σ corrected (filled circles) relative intensity of Se 3p to S 2p at different photon energies. The error bars represent the errors in the intensity ratios estimated from the errors in the decomposition of the experimental photoelectron spectra. The region shaded in green shows the region over which the fitting of the experimental intensity ratio was performed, and the red solid line shows the best fitting. **b** Modeled structure, which gives the best agreement with the experimentally obtained results from XPS, TEM, and ICP-AES. **c** Variation of the number density of S (dark yellow) and Se (orange) as a function of the radius of the nanoparticles for the best fit structure. (Adapted from [117])

In the specific example of CdS/CdSe core-shell sample, the $\sigma(h\nu)$ corrected intensity ratio I_{Se}/I_S decreases with increase in $h\nu$ (solid circles in Fig. 13.8a) qualitatively suggesting that the Se is relatively more abundant on the outer regions of the nanoparticle and S is present deeper towards the core, as targeted in the synthesis [117].

It is possible to obtain a quantitative description of the internal structure of these CdS/CdSe inverted core/shell nanoparticles by determining $N_S(r)$ and $N_{Se}(r)$ that would be consistent with the experimentally observed dependence of I_{Se}/I_S on $h\nu$, shown in Fig. 13.8a. By proper modeling of $N_S(r)$ and $N_{Se}(r)$ to simulate the experimentally obtained I_{Se}/I_S using (13.8), the quantitative structure was found [117] to have a core consisting of pure CdS followed by a gradient alloy of CdS and CdSe as shown as a schematic in Fig. 13.8b, c shows the variation of $N_S(r)$ and $N_{Se}(r)$ as a function of, r , the radial distance from the center of the nanoparticle to the surface. The calculated intensity variation for this particular structure is shown by the solid red line in Fig. 13.8a, which matches very well with the $\sigma(h\nu)$ corrected experimental intensity variation shown by the filled circles. The total size obtained from TEM and the overall chemical composition determined independently from ICP-AES match well with the quantitative model obtained from the analysis of the XPS data, firmly establishing the efficacy of using variable photon energy up to hard X-ray to determine the internal structure of such large sized nanoparticles [117].

13.8 Heterostructure Determination of Thin Films

Heterostructure determination by variable energy XPS can be easily extended to any structure with a spatial homogeneity along the x and y directions, representing a two-dimensionally homogeneous system and any arbitrary variation along the z direction; in other words, the number density function $N(x, y, z)$ appearing in (13.3) or in (13.6) can be replaced by $N(z)$, which is only a function of z . The depth into the material that can be probed and $N(z)$ determined in such a heterostructure is naturally limited by the mean free path, λ , of the photoelectron, indicating the obvious merit of employing hard X-ray photoemission spectroscopy in such cases. A beautiful demonstration [118] of this powerful technique with hard X-ray sources has been realized recently in determining the position of the two dimensional electron gas (2DEG) formed at the interface of two insulating oxides LaAlO_3 (LAO) and SrTiO_3 (STO). In the original discovery of this phenomenon [48], it was proposed that the polar discontinuity present across the SrTiO_3 – LaAlO_3 interface results in a diverging potential with a growing thickness of LAO, leading to electron transfers from the top LaAlO_3 layer to the interface SrTiO_3 layer at a critical thickness of LAO [45, 90], leading to the observed 2DEG carriers at the interface.

In order to demonstrate the efficacy of HAXPES in probing quantitatively the internal structure of such heterostructured oxide materials [52, 57, 59, 90, 118–121], we describe in some details results obtained in [118]. We show the variation in the La 3d/Sr 3d intensity ratio ($I_{\text{La}}/I_{\text{Sr}}$) corrected for the photoemission cross-section as a function of the photon energy in Fig. 13.9a for two samples, denoted as 6H and 6L. Here the number 6 corresponds to the targeted number of LAO unit cells (uc) grown on top of STO and H and L denote high and low oxygen partial pressure ($p\text{O}_2$), respectively, at the time of the growth of the STO and LAO layers. The 6H sample, grown at 10^{-4} Torr $p\text{O}_2$ is known to have a very low concentration of doped electrons [118], thereby serving the purpose of a reference sample; on the contrary, the 6L sample grown at 10^{-7} Torr $p\text{O}_2$ is known to be highly conducting with a large concentration of doped electrons [118]. The decreasing $\sigma(h\nu)$ corrected $I_{\text{La}}/I_{\text{Sr}}$ with an increasing $h\nu$ in Fig. 13.9a in conjunction with the experimental geometry defined in the inset implies LAO is indeed the over-layer and a systematic increase in $h\nu$ makes increasing depth into STO to become visible to the HAXPES technique, thereby increasing the Sr 3d intensity and decreasing $I_{\text{La}}/I_{\text{Sr}}$. Knowing that there are 6 layers of LAO on top of STO, the experimental geometry allows one to calculate the expected variation in the $\sigma(h\nu)$ corrected $I_{\text{La}}/I_{\text{Sr}}$ as a function of $h\nu$ using (13.6). This calculated curve is shown in Fig. 13.9a as green shade, with the width of the band arising from estimated errors in calculating the intensity ratio due to uncertainties in α , thickness of the LAO layer etc. Evidently, the calculated dependence and the experimentally obtained values are in excellent agreement, validating the approach and the data analysis.

Electrons doped in SrTiO_3 is necessarily accommodated in the Ti 3d conduction band of SrTiO_3 , thereby showing up as a Ti^{3+} spectral signature in contrast to Ti^{4+} spectral feature of undoped SrTiO_3 . Since the Ti^{3+} spectral features, with a lower

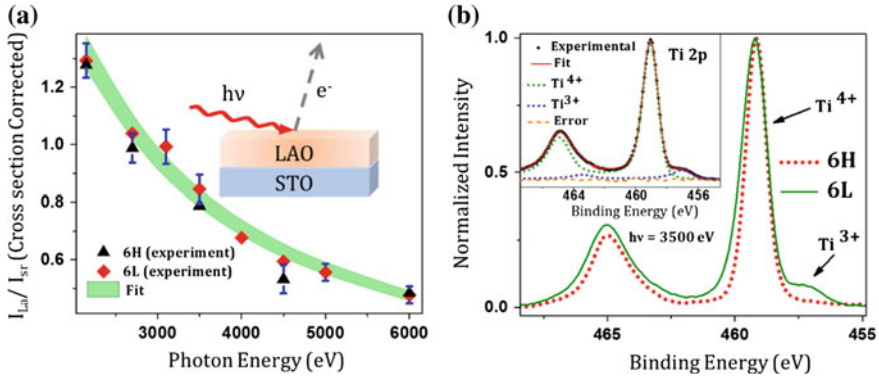


Fig. 13.9 **a** Experimentally obtained intensity ratio between La 3d and Sr 3d core levels spectra as a function of $h\nu$ for 6H and 6L samples are shown as *triangles* and *diamonds* respectively. The *blue bars* represent typical errors in the estimation of the intensity ratio. Simulation of the experimentally obtained intensity ratio between La 3d and Sr 3d of 6 uc samples to obtain the thickness of the *top* LAO layer is shown as *green shade*. **b** High resolution X-ray photoelectron spectra of Ti 2p core levels collected from the high pO_2 grown (6H) and low pO_2 grown (6L) samples with $h\nu = 3500$ eV. The *inset* of Fig. 13.9b shows the decomposition of the Ti 2p spectra collected from 6L sample at $h\nu = 3500$ eV to obtain the intensity of the Ti^{4+} and Ti^{3+} components. (Adapted from [118])

BE than those of Ti^{4+} are distinctly observed in Ti 2p spectra, it can be used to map the spatial distribution of doped carriers in the sample. Ti 2p core level spectra collected from 6L and 6H LAO-STO samples with $h\nu = 3500$ eV are shown in the main frame of Fig. 13.9b. The presence of Ti^{3+} feature at the lower BE side of the main Ti^{4+} peak only for the 6L sample with a charge carrier concentration $\sim 10^{17} \text{ cm}^{-2}$ (obtained from Hall measurements [118]) is clearly visible in comparison to the spectrum from the 6H reference sample. The inset to Fig. 13.9b shows the decomposition of the Ti 2p spectrum from the 6L sample in terms of its Ti^{3+} and Ti^{4+} contributions, allowing a quantitative estimate of Ti^{3+}/Ti^{4+} intensity ratio $I_{Ti^{3+}}/I_{Ti^{4+}}$ observed at different $h\nu$. One may at once anticipate that a systematic increase of $h\nu$ will allow us to explore how $I_{Ti^{3+}}/I_{Ti^{4+}}$ changes as we probe increasingly deeper into the heterostructure, thereby allowing us to map out how Ti^{3+} , or in other words the doped electron in $SrTiO_3$ is distributed as a function of the depth from the LAO-STO interface. It is interesting to note here that this intensity ratio, involving the same core level (2p) of the same element (Ti), does not require any correction from changes in the cross-sections with $h\nu$, as this quantity varies exactly the same way for Ti^{3+} and Ti^{4+} , and therefore, cancelling each other and consequently, reducing the uncertainty in the analysis [see (13.7)]. The absolute variation of $I_{Ti^{3+}}/I_{Ti^{4+}}$ for the 6L sample with $h\nu$ is shown in Fig. 13.10a. The gentle decrease in $I_{Ti^{3+}}/I_{Ti^{4+}}$ qualitatively suggests the presence of Ti^{3+} closer to the surface. When an attempt is made to describe the doped electron distribution as a single function at the interface, such as a Gaussian, Lorentzian or a rectangular function, with any arbitrary width, the best description obtained for $I_{Ti^{3+}}/I_{Ti^{4+}}$ as a

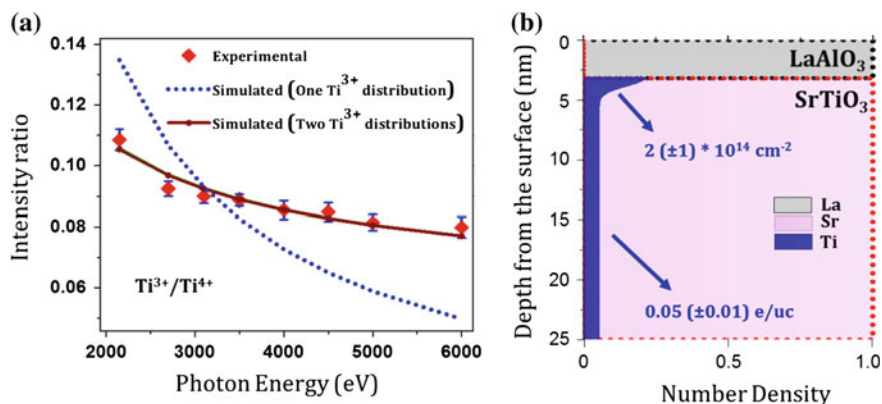


Fig. 13.10 a Intensity ratio (*red squares*) between Ti^{3+} and Ti^{4+} obtained from the decomposition of Ti 2p photoelectron spectra obtained from 6L samples at various photon energies. The errors in obtaining the intensity ratio are marked as *blue bars*. The wine *solid lines* shows the best fit to these intensity ratio. Ti^{3+} concentration distributions (*blue shade*) within the LAO-STO samples, that gives the best fitting to the experimentally obtained intensity ratios, are shown in Fig. 13.10b for 6L sample. The color code *grey* and *light pink* represents the LAO and STO layers, respectively, as obtained from the simulation of I_{La}/I_{Sr} intensity ratio. (Adapted from [118]) (Color figure online)

function of $h\nu$ is shown in Fig. 13.10a as the blue dotted line [118]. Clearly such a single distribution of the electron gas is grossly inadequate to describe the experimental data that exhibit a much weaker dependency on $h\nu$. Interestingly, the experimental data can be very well described when we assume two separate electron distributions (bimodal distribution), as shown by the good agreement between the calculated behavior (shown by the solid lines) and experimental data (filled diamonds). The corresponding bimodal charge carrier distribution within the sample is shown in Fig. 13.10b. This figure shows that a charge carrier distribution is tied to the interface with approximately $2 \times 10^{14} \text{ cm}^{-2}$ density, whereas the other charge carrier distribution appears to be an almost homogeneous bulk doping of STO with about 0.05 electrons per unit cell. Evidently, there is no other technique that can provide such critical and detailed information on these unusual systems with extraordinary properties.

The variable high-energy photoemission spectroscopic measurements have recently been used [122–125] to understand the interface structure of a magnetic tunnel junction (MTJ) consisting of thin CoFeB (CFB) layers as ferromagnetic electrodes and MgO as the insulating layer in-between. In the following, we describe results from [125] to underline the ability of HAXPES to provide quantitative description of internal structures even in such complex, multicomponent systems. The overall structure of the two MTJ investigated consists of the stacking as Si(substrate)/Ta(5)/Ru(10)/Ta(5)/ $Co_{20}Fe_{60}B_{20}$ (5)/MgO(2) with the numbers in the brackets indicating the thickness of the corresponding layers in nm. High energy photoemission spectra collected for Fe 2p and B 1s at $h\nu$ between 2500 and

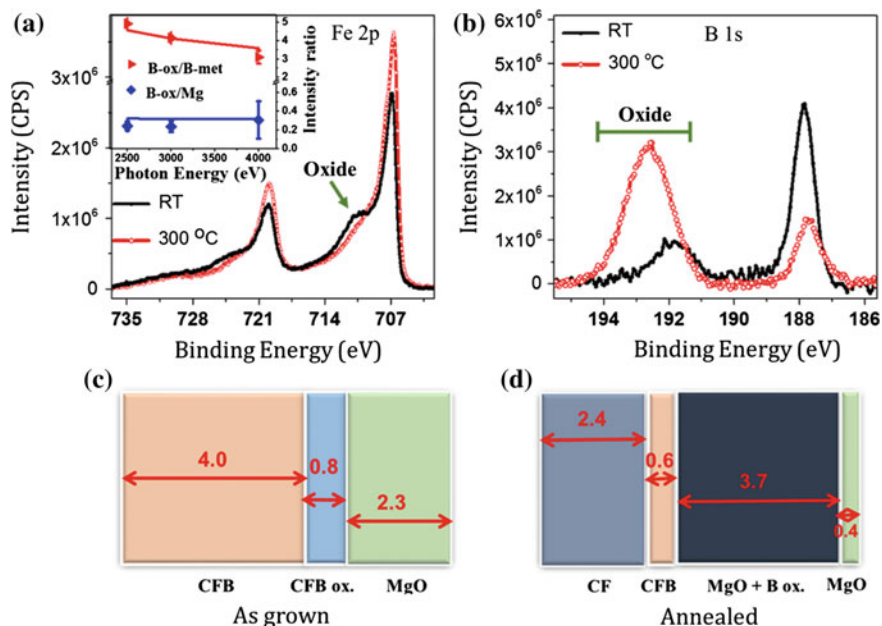


Fig. 13.11 a and b show Fe 2p and B 1s core level spectra collected from the uncapped bilayer MTJ sample at $h\nu = 3000$ eV photon energy before (black) and after (red) annealing the sample at 300 ± 5 °C for 20 min. The inset of Fig. 13.11a shows the intensity ratio between B-oxide to B-metal (red triangles) and B-oxide to Mg (blue square) obtained from 300 ± 5 °C annealed sample at different photon energies. The lines represent the simulated intensity ratios for the best fitted structure, shown in Fig. 13.11d. The thickness and nature of various layers in the unannealed and annealed uncapped bilayer sample are shown in Fig. 13.11c, d. The numbers shown in the figures are in nanometer. (Adapted from [125])

4000 eV from this MTJ sample are shown in Fig. 13.11a, b, respectively, for two different cases. First, the sample as grown was investigated; then the sample was annealed at 300 °C for 20 min to understand the effect of annealing that is involved in processing of MTJ layers for device applications. This annealed sample was also investigated in an identical manner to understand the consequence of annealing [125]. The spin-orbit split metallic peaks of Fe 2p can be seen at BE of 706.8 and 720 eV and the B 1s metallic peak appears at BE of 187.8 eV. Along with the characteristic metallic features, both Fe 2p and B 1s spectra contain additional features at higher binding energies arising from corresponding oxide species, as indicated in the Figs. 13.10b, 13.11a. For Fe 2p, the oxide species appears at 3.6 eV higher BE from the main peaks, whereas it is at BE of about 191.8 eV for B 1s. The intensity ratio of the B-oxide and B-metallic 1s peak for the annealed sample is shown in the inset to Fig. 13.11a as a function of $h\nu$. It is clear from this plot that the intensity of the oxide species decreases with respect to the metallic peak when the spectra are collected with higher photon energies, suggesting presence of the oxide species closer to the surface compared to the metallic counterparts; a similar

observation was also made for the Fe-oxide signal. Such intensity ratios, not only for the oxide and metallic signals of the same elements, but also spectral intensity of different elements, such as B-oxide 1s/Mg 1s (shown in the inset to Fig. 13.11a for the annealed sample), Fe 2p/Mg 1s, Fe 2p/Co 2p (not shown here) were also obtained in this study for both samples as a function of the $h\nu$. These experimentally obtained intensity variations with the photon energy help to understand the internal structure of these two samples in detail [125]. For example, the relative insensitivity of the B-oxide/Mg intensity ratio on $h\nu$ for the annealed sample shown in the inset suggests that boron oxide is spread nearly homogeneously in the MgO layer, as has also been reported in [122, 123]. Taking into account the intensity variation of various core levels at different photon energies, it was possible to obtain a quantitative description of the internal structure [125] of this bilayer MTJ sample before and after annealing, as shown in Fig. 13.11c and d, respectively. This study also reports the internal structure of a tri-layer sample (with an additional $C_{20}F_{60}B_{20}$ layer on top of MgO), in contrast to the bilayered one discussed here, resolving controversy on the behavior of B diffusion on annealing the sample, illustrating the tremendous usefulness of this technique.

13.9 Conclusion and Future Outlook

In this chapter, we have detailed how one may extract in-depth knowledge of the internal geometric and electronic structures of heterogeneous materials with the use of variable photon energy available at synchrotron radiation centers to carry out depth resolved X-ray photoelectron spectroscopy. Competing techniques to obtain such information are typically based on microscopic approaches, such as transmission electron microscopy (TEM) together with its ability to perform space resolved elemental identification via energy dispersive X-ray analysis and electron energy loss spectroscopy, and scanning tunneling microscopy (STM). In general, STM is extremely surface sensitive and it is impossible to obtain depth resolved information from such a technique. There have been attempts reported in the literature to obtain information beyond the surface by carrying out cross-sectional studies; this requires cutting through the sample in a direction perpendicular to the surface, thereby exposing the deeper part of the sample to the STM probe. However, strictly speaking, any information so obtained continues to be a surface related information, since the act of making the cross-sectional cut introduces a new surface in the sample. Since the surface electronic structure may be different from those from beyond the surface, cross-sectional studies to that extent may alter the electronic structure being probed compared to that in the deeper part of the system in an uncontrolled manner. This may limit the usefulness and applicability of such cross-sectional studies. Similar cross-sectional studies are also popular in conjunction with TEM. Obvious advantage of the technique discussed here based on photoelectron spectroscopy is its nondestructive nature. It has the ability of investigating the sample as such without the need to introduce any new surfaces to

access deeper parts of the sample. The other advantage of the present technique is that it naturally provides depth (or vertically) resolved information into the sample, starting from the surface, with the help of a changing mean free path of photoelectrons with a change in their kinetic energy brought about by changing the photon energy; this is in contrast to the laterally resolved information from all microscopic techniques mentioned above. Of course, there are several limitations of the present technique as well. For example, the depth that can be probed effectively using this technique is limited severely by ultra-short mean free paths of photoelectrons. Even with the advent of hard X-rays up to about 10 keV to carry out photoelectron spectroscopy, it is not possible to reliably probe beyond a depth of $\sim 15\text{--}20$ nm. We note that this is not a limitation on the sample thickness; even a macroscopically thick sample may be investigated without any need to thin down the sample unlike in the case of TEM. However, the depth-resolved information will be restricted to within the first 15–20 nm of the surface at best using this technique. Since most of the nanocrystals investigated have sizes below 20 nm, the present technique is an ideal tool to probe their internal structures. Also, any heterostructures can be probed as long as the interface of interest is not buried deeper than the above-mentioned limit, as discussed in specific examples in this chapter.

It is important to keep in mind the uncertainties inherent in this technique. As has been explained in detail, a quantitative determination of the internal structure of any sample requires the knowledge of several parameters that are not very well controlled, thereby introducing uncertainties in the derived quantitative estimates. One such uncertainty arises from the estimate of the mean free path which is never easy to determine a priori with a great accuracy. The second source of uncertainty is the photon energy dependent cross-section of various levels that are analyzed to extract the depth resolved information. Other parameters, such as the photon flux and other experimental factors, can be largely taken care of by analyzing only intensity ratios and opting for core level signals that have similar binding energies, as explained in this chapter. It is also to be realized that the analysis of the intensity ratio as a function of the photon energy to extract the internal structure is based on a presumed parameterized model of the internal structure, such that the internal parameters of the assumed model are optimized to provide the best description of the intensity variation. Thus, the analysis can be hoped to provide reasonable estimates only if the assumed model is realistic. This implies that it is important to have some basic ideas of the shape and the internal symmetry of the sample.

The above mentioned limitations point to the fact that the present technique, instead of being viewed as a competing technique, should be more viewed as a complimentary one to other techniques that can provide any clue to the internal structure. Thus, it is important to start the analysis with a prior knowledge of the shape and overall dimension of the sample in case of nanomaterials. This information is easily obtained from TEM studies and helps to build up the model for the analysis. Similarly, in many spherical nanocrystals synthesized via the solution route, it is also reasonable to assume a spherical symmetry of the composition, helping to bring down the number of parameters in the model. The overall size

determined from the TEM study then provides a critical test for the model, since the analysis of the photoelectron spectroscopic results must be consistent with that of TEM in terms of the total size of the nanocrystal. Similarly, elemental analysis using ICP-AES or atomic absorption spectroscopy provides important restrictions on the model, since each optimized model corresponds to a well-defined average composition. Using every such available information on the system, one may substantially reduce the uncertainties associated with the analysis of the internal structure based on the present technique.

Since the electronic structure of any material is crucially dependent on the elemental distribution within the sample, it is clear that understanding the internal structure of low dimensional systems is of great importance, as has been discussed in this chapter. With an increasing number of beamlines becoming available around the world where one may carry out high resolution photoelectron spectroscopy over a wide range of photon energies, it appears that this technique, in conjunction with all other complimentary techniques, will play a unique and powerful role in unraveling the internal geometric and electronic structures of such systems.

References

1. G. Schmid (ed.), *Nanoparticles: From Theory to Application*, 2nd edn (Wiley-VCH Verlag GmbH & Co. KGaA: Weinheim, Germany, 2010)
2. H. Weller, Colloidal semiconductor Q-particles: chemistry in the transition region between solid state and molecules. *Angew. Chem. Int. Ed. Engl.* **32**(1), 41–53 (1993)
3. D. Bera et al., Quantum dots and their multimodal applications: a review. *Materials* **3**(4), 2260–2345 (2010)
4. T. Trindade, P. O'Brien, N.L. Pickett, Nanocrystalline semiconductors: synthesis, properties, and perspectives. *Chem. Mater.* **13**(11), 3843–3858 (2001)
5. B.O. Dabbousi et al., (CdSe)ZnS core-shell quantum dots: synthesis and characterization of a size series of highly luminescent nanocrystallites. *J. Phys. Chem. B* **101**(46), 9463–9475 (1997)
6. S. Sapra, D.D. Sarma, Evolution of the electronic structure with size in II–VI semiconductor nanocrystals. *Phys. Rev. B* **69**(12), 125304 (2004)
7. C.B. Murray, D.J. Norris, M.G. Bawendi, Synthesis and characterization of nearly monodisperse CdE (E = sulfur, selenium, tellurium) semiconductor nanocrystallites. *J. Am. Chem. Soc.* **115**(19), 8706–8715 (1993)
8. R. Viswanatha, D.D. Sarma, Study of the growth of capped ZnO nanocrystals: a route to rational synthesis. *Chem. A Eur. J.* **12**(1), 180–186 (2006)
9. X. Peng et al., Shape control of CdSe nanocrystals. *Nature* **404**(6773), 59–61 (2000)
10. C.J. Murphy, N.R. Jana, Controlling the aspect ratio of inorganic nanorods and nanowires. *Adv. Mater.* **14**(1), 80–82 (2002)
11. S. Acharya et al., Shape-dependent confinement in ultrasmall zero-, one-, and two-dimensional PbS nanostructures. *J. Am. Chem. Soc.* **131**(32), 11282–11283 (2009)
12. C. Burda et al., Chemistry and properties of nanocrystals of different shapes. *Chem. Rev.* **105**(4), 1025–1102 (2005)
13. A.R. Tao, S. Habas, P. Yang, Shape control of colloidal metal nanocrystals. *Small* **4**(3), 310–325 (2008)

14. M.A. Hines, P. Guyot-Sionnest, Synthesis and characterization of strongly luminescing ZnS-capped CdSe nanocrystals. *J. Phys. Chem.* **100**(2), 468–471 (1996)
15. X. Peng et al., Epitaxial growth of highly luminescent CdSe/CdS core/shell nanocrystals with photostability and electronic accessibility. *J. Am. Chem. Soc.* **119**(30), 7019–7029 (1997)
16. J.-S. Lee, E.V. Shevchenko, D.V. Talapin, Au–PbS core-shell nanocrystals: plasmonic absorption enhancement and electrical doping via intra-particle charge transfer. *J. Am. Chem. Soc.* **130**(30), 9673–9675 (2008)
17. P. Reiss, J. Bleuse, A. Pron, Highly luminescent CdSe/ZnSe core/shell nanocrystals of low size dispersion. *Nano Lett.* **2**(7), 781–784 (2002)
18. P. Reiss, M. Protière, L. Li, Core/shell semiconductor nanocrystals. *Small* **5**(2), 154–168 (2009)
19. D.D. Sarma et al., Origin of the enhanced photoluminescence from semiconductor CdSeS nanocrystals. *J. Phys. Chem. Lett.* **1**(14), 2149–2153 (2010)
20. P.K. Santra et al., Investigation of the internal heterostructure of highly luminescent quantum dot—quantum well nanocrystals. *J. Am. Chem. Soc.* **131**(2), 470–477 (2008)
21. A. Eychmüller, A. Mews, H. Weller, A quantum dot quantum well: CdS/HgS/CdS. *Chem. Phys. Lett.* **208**(1–2), 59–62 (1993)
22. D. Battaglia, B. Blackman, X. Peng, Coupled and decoupled dual quantum systems in one semiconductor nanocrystal. *J. Am. Chem. Soc.* **127**(31), 10889–10897 (2005)
23. S. Sengupta et al., Long-range visible fluorescence tunability using component-modulated coupled quantum dots. *Adv. Mater.* **23**(17), 1998–2003 (2011)
24. J.J. Li et al., Large-scale synthesis of nearly monodisperse CdSe/CdS core/shell nanocrystals using air-stable reagents via successive ion layer adsorption and reaction. *J. Am. Chem. Soc.* **125**(41), 12567–12575 (2003)
25. U. Resch-Genger et al., Quantum dots versus organic dyes as fluorescent labels. *Nat. Meth.* **5**(9), 763–775 (2008)
26. A.B. Greytak et al., Alternating layer addition approach to CdSe/CdS core/shell quantum dots with near-unity quantum yield and high on-time fractions. *Chem. Sci.* **3**(6), 2028–2034 (2012)
27. J.-S. Lee et al., “Magnet-in-the-semiconductor” FePt–PbS and FePt–PbSe nanostructures: magnetic properties, charge transport, and magnetoresistance. *J. Am. Chem. Soc.* **132**(18), 6382–6391 (2010)
28. R. Ghosh Chaudhuri, S. Paria, Core/shell nanoparticles: classes, properties, synthesis mechanisms, characterization, and applications. *Chem. Rev.* **112**(4), 2373–2433 (2011)
29. S. Kim et al., Type-II quantum dots: CdTe/CdSe(Core/Shell) and CdSe/ZnTe(Core/Shell) heterostructures. *J. Am. Chem. Soc.* **125**(38), 11466–11467 (2003)
30. R.E. Bailey, S. Nie, Alloyed semiconductor quantum dots: tuning the optical properties without changing the particle size. *J. Am. Chem. Soc.* **125**(23), 7100–7106 (2003)
31. X. Zhong et al., Alloyed $Zn_xCd_{1-x}S$ nanocrystals with highly narrow luminescence spectral width. *J. Am. Chem. Soc.* **125**(44), 13559–13563 (2003)
32. A. Nag, S. Chakraborty, D.D. Sarma, To dope Mn^{2+} in a semiconducting nanocrystal. *J. Am. Chem. Soc.* **130**(32), 10605–10611 (2008)
33. H. Borchert et al., Photoemission study of onion like quantum dot quantum well and double quantum well nanocrystals of CdS and HgS. *J. Phys. Chem. B* **107**(30), 7486–7491 (2003)
34. S. Sapra et al., Bright white-light emission from semiconductor nanocrystals: by chance and by design. *Adv. Mater.* **19**(4), 569–572 (2007)
35. F. García-Santamaría et al., Breakdown of volume scaling in auger recombination in CdSe/CdS heteronanocrystals: the role of the core-shell interface. *Nano Lett.* **11**(2), 687–693 (2011)
36. N. Tschirner et al., Interfacial alloying in CdSe/CdS heteronanocrystals: a raman spectroscopy analysis. *Chem. Mater.* **24**(2), 311–318 (2011)
37. W.K. Bae et al., Controlled alloying of the core-shell interface in CdSe/CdS quantum dots for suppression of auger recombination. *ACS Nano* **7**(4), 3411–3419 (2013)

38. X. Wang et al., Non-blinking semiconductor nanocrystals. *Nature* **459**(7247), 686–689 (2009)
39. M. Benoit et al., Towards non-blinking colloidal quantum dots. *Nat. Mater.* **7**(8), 659–664 (2008)
40. J. Mathon, A. Umerski, Theory of tunneling magnetoresistance of an epitaxial Fe/MgO/Fe (001) junction. *Phys. Rev. B* **63**(22), 220403 (2001)
41. C. Tusche et al., Oxygen-induced symmetrization and structural coherency in Fe/MgO/Fe (001) magnetic tunnel junctions. *Phys. Rev. Lett.* **95**(17), 176101 (2005)
42. F. Bonell et al., Spin-polarized electron tunneling in bcc FeCo/MgO/FeCo (001) magnetic tunnel junctions. *Phys. Rev. Lett.* **108**(17), 176602 (2012)
43. S. Ikeda et al., Tunnel magnetoresistance of 604 % at 300 K by suppression of Ta diffusion in CoFeB/MgO/CoFeB pseudo-spin-valves annealed at high temperature. *Appl. Phys. Lett.* **93**(8) (2008)
44. S.S.P. Parkin et al., Giant tunnelling magnetoresistance at room temperature with MgO (100) tunnel barriers. *Nat. Mater.* **3**(12), 862–867 (2004)
45. H.Y. Hwang et al., Emergent phenomena at oxide interfaces. *Nat. Mater.* **11**(2), 103–113 (2012)
46. J. Chakhalian, A.J. Millis, J. Rondinelli, Whither the oxide interface. *Nat. Mater.* **11**(2), 92–94 (2012)
47. A. Tsukazaki et al., Quantum hall effect in polar oxide heterostructures. *Science* **315**(5817), 1388–1391 (2007)
48. A. Ohtomo, H.Y. Hwang, A high-mobility electron gas at the LaAlO₃/SrTiO₃ heterointerface. *Nature* **427**(6973), 423–426 (2004)
49. N. Reyren et al., Superconducting interfaces between insulating oxides. *Science* **317**(5842), 1196–1199 (2007)
50. A. Brinkman et al., Magnetic effects at the interface between non-magnetic oxides. *Nat. Mater.* **6**(7), 493–496 (2007)
51. M. Gorgoi et al., The high kinetic energy photoelectron spectroscopy facility at BESSY progress and first results. *Nucl. Instrum. Methods Phys. Res. Sect. A* **601**(1–2), 48–53 (2009)
52. R. Knut et al., High energy photoelectron spectroscopy in basic and applied science: Bulk and interface electronic structure. *J. Electron Spectrosc. Relat. Phenom.* **190**(Part B 0), 278–288 (2013)
53. S. Ueda, Application of hard X-ray photoelectron spectroscopy to electronic structure measurements for various functional materials. *J. Electron Spectrosc. Relat. Phenom.* **190**(Part B 0), 235–241 (2013)
54. E. Ikenaga et al., Development of high lateral and wide angle resolved hard X-ray photoemission spectroscopy at BL47XU in SPring-8. *J. Electron Spectrosc. Relat. Phenom.* **190**(Part B 0), 180–187 (2013)
55. D. Céolin et al., Hard X-ray photoelectron spectroscopy on the GALAXIES beamline at the SOLEIL synchrotron. *J. Electron Spectrosc. Relat. Phenom.* **190**(Part B 0), 188–192 (2013)
56. H. Wadati, A. Fujimori, Hard X-ray photoemission spectroscopy of transition-metal oxide thin films and interfaces. *J. Electron Spectrosc. Relat. Phenom.* **190**(Part B 0), 222–227 (2013)
57. R. Claessen et al., Hard X-ray photoelectron spectroscopy of oxide hybrid and heterostructures: a new method for the study of buried interfaces. *New J. Phys.* **11**, 125007 (2009)
58. F. Borgatti et al., Interfacial and bulk electronic properties of complex oxides and buried interfaces probed by HAXPES. *J. Electron Spectrosc. Relat. Phenom.* **190**(Part B 0), 228–234 (2013)
59. C. Caspers et al., Chemical stability of the magnetic oxide EuO directly on silicon observed by hard X-ray photoemission spectroscopy. *Phys. Rev. B* **84**(20), 205217 (2011)
60. M. Gorgoi et al., Hard X-ray high kinetic energy photoelectron spectroscopy at the KMC-1 beamline at BESSY. *Eur. Phys. J. Special Topics* **169**(1), 221–225 (2009)

61. C. Weiland et al., NIST high throughput variable kinetic energy hard X-ray photoelectron spectroscopy facility. *J. Electron Spectrosc. Relat. Phenom.* **190**(Part B 0), 193–200 (2013)
62. S. Hufner, *Photoelectron Spectroscopy, Principles and Applications* (Springer, Berlin, New York, 1995)
63. K. Siegbahn et al., ESCA: atomic, molecular, and solid state structure studies by means of electron spectroscopy. *Nova Acta Regiae Soc. Sci. Ups. Ser. IV*, 1967. 20
64. A. Fujimori et al., Core-level photoemission measurements of the chemical potential shift as a probe of correlated electron systems. *J. Electron Spectrosc. Relat. Phenom.* **124**(2–3), 127–138 (2002)
65. E. Hao et al., Synthesis and optical properties of CdSe and CdSe/CdS nanoparticles. *Chem. Mater.* **11**(11), 3096–3102 (1999)
66. I. Tunc et al., XPS characterization of Au (Core)/SiO₂ (Shell) nanoparticles. *J. Phys. Chem. B* **109**(16), 7597–7600 (2005)
67. P.A. Mangrulkar et al., Throwing light on platinized carbon nanostructured composites for hydrogen generation. *Energy Environ. Sci.* **7**(12), 4087–4094 (2014)
68. H. Jensen et al., XPS and FTIR investigation of the surface properties of different prepared titania nano-powders. *Appl. Surf. Sci.* **246**(1–3), 239–249 (2005)
69. J.S. Owen et al., Reaction chemistry and ligand exchange at cadmium–selenide nanocrystal surfaces. *J. Am. Chem. Soc.* **130**(37), 12279–12281 (2008)
70. A. Roy et al., Photoemission study of porous silicon. *Appl. Phys. Lett.* **61**(14), 1655–1657 (1992)
71. A. Roy, D.D. Sarma, A.K. Sood, Spectroscopic studies on quantum dots of PbI₂. *Spectrochim. Acta Part A* **48**(11–12), 1779–1787 (1992)
72. J. Jasieniak, P. Mulvaney, From Cd-rich to Se-rich—the manipulation of CdSe nanocrystal surface stoichiometry. *J. Am. Chem. Soc.* **129**(10), 2841–2848 (2007)
73. J.E.B. Katari, V.L. Colvin, A.P. Alivisatos, X-ray photoelectron spectroscopy of CdSe nanocrystals with applications to studies of the nanocrystal surface. *J. Phys. Chem.* **98**(15), 4109–4117 (1994)
74. U. Winkler et al., Detailed investigation of CdS nanoparticle surfaces by high-resolution photoelectron spectroscopy. *Chem. Phys. Lett.* **306**(1–2), 95–102 (1999)
75. S.K. Kulkarni et al., Investigations on chemically capped CdS, ZnS and ZnCdS nanoparticles. *Appl. Surf. Sci.* **169–170**, 438–446 (2001)
76. K.B. Subila et al., Luminescence properties of CdSe quantum dots: role of crystal structure and surface composition. *J. Phys. Chem. Lett.* **4**(16), 2774–2779 (2013)
77. V. Vijayakrishnan et al., Metal-insulator transitions in metal clusters: a high-energy spectroscopy study of palladium and silver clusters. *J. Phys. Chem.* **96**(22), 8679–8682 (1992)
78. B.M. Reddy, B. Chowdhury, P.G. Smirniotis, An XPS study of the dispersion of MoO₃ on TiO₂–ZrO₂, TiO₂–SiO₂, TiO₂–Al₂O₃, SiO₂–ZrO₂, and SiO₂–TiO₂–ZrO₂ mixed oxides. *Appl. Catal. A* **211**(1), 19–30 (2001)
79. N. Kruse, S. Chenakin, XPS characterization of Au/TiO₂ catalysts: Binding energy assessment and irradiation effects. *Appl. Catal. A* **391**(1–2), 367–376 (2011)
80. A.V. Baranov et al., Effect of ZnS shell thickness on the phonon spectra in CdSe quantum dots. *Phys. Rev. B* **68**(16), 165306 (2003)
81. F. Todescato et al., Investigation into the heterostructure interface of CdSe-based core-shell quantum dots using surface-enhanced raman spectroscopy. *ACS Nano* **7**(8), 6649–6657 (2013)
82. W.W. Yu et al., Experimental determination of the extinction coefficient of CdTe, CdSe, and CdS nanocrystals. *Chem. Mater.* **15**(14), 2854–2860 (2003)
83. S. Tougaard, Surface nanostructure determination by X-ray photoemission spectroscopy peak shape analysis. *J. Vac. Sci. Technol. A* **14**(3), 1415–1423 (1996)
84. I. Doron-Mor et al., Controlled surface charging as a depth-profiling probe for mesoscopic layers. *Nature* **406**(6794), 382–385 (2000)

85. B.J. Tyler, D.G. Castner, B.D. Ratner, Regularization: a stable and accurate method for generating depth profiles from angle-dependent XPS data. *Surf. Interface Anal.* **14**(8), 443–450 (1989)
86. S. Hajati, S. Tougaard, Non-Destructive depth profiling by XPS peak shape analysis. *J. Surf. Anal.* **15**(3), 220–224 (2009)
87. S.H. Yang et al., Depth-resolved photoemission spectroscopy with soft X-ray standing waves. *J. Electron Spectrosc. Relat. Phenom.* **114–116**, 1089–1095 (2001)
88. D.D. Sarma et al., X-ray photoelectron spectroscopy: a unique tool to determine the internal heterostructure of nanoparticles. *Chem. Mater.* **25**(8), 1222–1232 (2013)
89. E. Holmström et al., Sample preserving deep interface characterization technique. *Phys. Rev. Lett.* **97**(26), 266106 (2006)
90. M. Sing et al., Profiling the interface electron gas of $\text{LaAlO}_3/\text{SrTiO}_3$ heterostructures with hard X-ray photoelectron spectroscopy. *Phys. Rev. Lett.* **102**(17), 176805 (2009)
91. W.A.M. Aarnink, A. Weishaupt, A. van Silfhout, Angle-resolved X-ray photoelectron spectroscopy (ARXPS) and a modified Levenberg-Marquardt fit procedure: a new combination for modeling thin layers. *Appl. Surf. Sci.* **45**(1), 37–48 (1990)
92. C. Weiland et al., Nondestructive compositional depth profiling using variable-kinetic energy hard X-ray photoelectron spectroscopy and maximum entropy regularization. *Surf. Interface Anal.* **46**(6), 407–417 (2014)
93. T.A. Carlson, G.E. McGuire, Study of the X-ray photoelectron spectrum of tungsten—tungsten oxide as a function of thickness of the surface oxide layer. *J. Electron Spectrosc. Relat. Phenom.* **1**(2), 161–168 (1972)
94. L. Kumar, D.D. Sarma, S. Krummacher, XPS study of the room temperature surface oxidation of zirconium and its binary alloys with tin, chromium and iron. *Appl. Surf. Sci.* **32**(3), 309–319 (1988)
95. J. Nanda, B.A. Kuruvilla, D.D. Sarma, Photoelectron spectroscopic study of CdS nanocrystallites. *Phys. Rev. B* **59**(11), 7473–7479 (1999)
96. J. Nanda, D.D. Sarma, Photoemission spectroscopy of size selected zinc sulfide nanocrystallites. *J. Appl. Phys.* **90**(5), 2504–2510 (2001)
97. P. Sen et al., An electron spectroscopic study of the surface oxidation of glassy and crystalline Cu–Zr alloys. *J. Phys. F: Met. Phys.* **14**(2), 565–577 (1984)
98. D.A. Shirley, High-resolution X-ray photoemission spectrum of the valence bands of gold. *Phys. Rev. B* **5**(12), 4709–4714 (1972)
99. R. Hesse et al., Comparative study of the modelling of the spectral background of photoelectron spectra with the Shirley and improved Tougaard methods. *J. Electron Spectrosc. Relat. Phenom.* **186**, 44–53 (2013)
100. S. Tanuma, C.J. Powell, D.R. Penn, Calculations of electron inelastic mean free paths (IMFPs). IV. Evaluation of calculated IMFPs and of the predictive IMFP formula TPP-2 for electron energies between 50 and 2000 eV. *Surf. Interface Anal.* **20**(1), 77–89 (1993)
101. C.S. Fadley, S. Nemsák, Some future perspectives in soft- and hard-X-ray photoemission. *J. Electron Spectrosc. Relat. Phenom.* **195**, 409–422 (2014)
102. B. Pal, S. Mukherjee, D. D. Sarma, Probing internal structures using hard X-ray photoelectron spectroscopy (HAXPES). *J. Electron Spectrosc. Relat. Phenom.* **200**, (2015). doi: [10.1016/j.elspec.2015.06.005](https://doi.org/10.1016/j.elspec.2015.06.005)
103. S. Tanuma, C.J. Powell, D.R. Penn, Calculations of electron inelastic mean free paths for 31 materials. *Surf. Interface Anal.* **11**(11), 577–589 (1988)
104. S. Tanuma, C.J. Powell, D.R. Penn, Calculations of electron inelastic mean free paths. III. Data for 15 inorganic compounds over the 50–2000 eV range. *Surf. Interface Anal.* **17**(13), 927–939 (1991)
105. C. Cancellieri et al., Interface fermi states of $\text{LaAlO}_3/\text{SrTiO}_3$ and related heterostructures. *Phys. Rev. Lett.* **110**(13), 137601 (2013)
106. J.J. Yeh, I. Lindau, Atomic subshell photoionization cross sections and asymmetry parameters: $1 \leq Z \leq 103$. *At. Data Nucl. Data Tables* **32**(1), 1–155 (1985)

107. J. H. Scofield, Theoretical photoionization cross sections from 1 to 1500 keV. Lawrence Livermore National Laboratory Rep (1973)
108. R. Hesse, P. Streubel, R. Szargan, Improved accuracy of quantitative XPS analysis using predetermined spectrometer transmission functions with UNIFIT 2004. *Surf. Interface Anal.* **37**(7), 589–607 (2005)
109. S. Sapra et al., Unraveling internal structures of highly luminescent PbSe nanocrystallites using variable-energy synchrotron radiation photoelectron spectroscopy. *J. Phys. Chem. B* **110**(31), 15244–15250 (2006)
110. D. D. Sarma, P. Sen, XPS and Auger studies of the surface oxidation of Manganese. *Proc. Indian Natn. Sci. Acad.* **49**(A)(3) (1983)
111. P. Sen, M.S. Hegde, C.N.R. Rao, Surface oxidation of cadmium, indium, tin and antimony by photoelectron and Auger spectroscopy. *Appl. Surf. Sci.* **10**(1), 63–74 (1982)
112. D.D. Sarma, M.S. Hegde, C.N.R. Rao, Study of surface oxidation of rare-earth metals by photoelectron spectroscopy. *J. Chem. Soc. Faraday Trans. 2: Mol. Chem. Phys.* **77**(9), 1509–1520 (1981)
113. M. Ayyoob, D.D. Sarma, XPS and UVPES studies of the surface oxidation of Gd and Yb. *Ind. J. Chem.* **22** (A) (1983)
114. H. Borchert et al., Relations between the photoluminescence efficiency of CdTe nanocrystals and their surface properties revealed by synchrotron XPS. *J. Phys. Chem. B* **107**(36), 9662–9668 (2003)
115. F. Bernardi et al., Unraveling the formation of core-shell structures in nanoparticles by S-XPS. *J. Phys. Chem. Lett.* **1**(6), 912–917 (2010)
116. K. Huang et al., Internal structure of InP/ZnS nanocrystals unraveled by high-resolution soft X-ray photoelectron spectroscopy. *ACS Nano* **4**(8), 4799–4805 (2010)
117. S. Mukherjee et al., Determination of internal structures of heterogeneous nanocrystals using variable-energy photoemission spectroscopy. *J. Phys. Chem. C* **118**(28), 15534–15540 (2014)
118. S. Mukherjee et al., Distribution and nature of charge carriers in LaAlO₃-SrTiO₃ oxide heterostructures. Unpublished results
119. M. Paul et al., Probing the interface of Fe₃O₄GaAs thin films by hard X-ray photoelectron spectroscopy. *Phys. Rev. B* **79**(23), 233101 (2009)
120. E. Slooten et al., Hard X-ray photoemission and density functional theory study of the internal electric field in SrTiO₃/LaAlO₃ oxide heterostructures. *Phys. Rev. B* **87**(8), 085128 (2013)
121. C. Weiland et al., Hard X-ray photoelectron spectroscopy study of As and Ga out-diffusion in In_{0.53}Ga_{0.47}As/Al₂O₃ film systems. *Appl. Phys. Lett.* **101**(6), 061602 (2012)
122. A.A. Greer et al., Observation of boron diffusion in an annealed Ta/CoFeB/MgO magnetic tunnel junction with standing-wave hard X-ray photoemission. *Appl. Phys. Lett.* **101**(20), 202402 (2012)
123. A.K. Rumaiz et al., Boron migration due to annealing in CoFeB/MgO/CoFeB interfaces: a combined hard X-ray photoelectron spectroscopy and X-ray absorption studies. *Appl. Phys. Lett.* **99**(22), 222502 (2011)
124. X. Kozina et al., A nondestructive analysis of the B diffusion in Ta–CoFeB–MgO–CoFeB–Ta magnetic tunnel junctions by hard X-ray photoemission. *Appl. Phys. Lett.* **96**(7), 072105 (2010)
125. S. Mukherjee et al., Role of boron diffusion in CoFeB/MgO magnetic tunnel junctions. *Phys. Rev. B* **91**(8), 085311 (2015)